CORRECTION POSTED 7 SEPTEMBER 2023

SOFT ROBOTS

Increasing the payload capacity of soft robot arms by localized stiffening

Daniel Bruder*, Moritz A. Graule, Clark B. Teeple, Robert J. Wood

Soft robot arms offer safety and adaptability due to their passive compliance, but this compliance typically limits their payload capacity and prevents them from performing many tasks. This paper presents a model-based design approach to effectively increase the payload capacity of soft robot arms. The proposed approach uses localized body stiffening to decrease the compliance at the end effector without sacrificing the robot's range of motion. This approach is validated on both a simulated and a real soft robot arm, where experiments show that increasing the stiffness of localized regions of their bodies reduces the compliance at the end effector and increases the height to which the arm can lift a payload. By increasing the payload capacity of soft robot arms, this approach has the potential to improve their efficacy in a variety of tasks including object manipulation and exploration of cluttered environments.

INTRODUCTION

Compliance, the extent to which a structure deforms because of an applied load, increases safety by mitigating the damage caused by large contact forces through deformation. In robot arms, compliance is essential for ensuring safe execution of tasks that involve physical human-robot interactions, such as bathing (*1*, *2*) and feeding (*3*), manipulating delicate objects (*4*–*8*), and maneuvering in unknown environments (*9*–*12*).

Compliance can be achieved via control or structure, and each paradigm has unique advantages and disadvantages. Compliance achieved via control can be tuned without making physical alterations to a robot but requires accurate sensing and high-bandwidth feedback. Compliance achieved via structure, specifically because of the passive compliance of a robot's body, does not require such hardware but can only be tuned by modifying the morphology of the robot itself.

Traditional rigid-bodied robots tend to achieve compliance via control. They are composed of rigid links and use rigid actuators, such as motors, which constrain motion to occur only along the actuated degree of freedom. Rigid-bodied robots that use such actuators at all of their joints are considered fully actuated. Fully actuated robots are able to achieve compliance by using feedback to react to external forces in a way that mimics the behavior of a more inherently compliant system, and there are a number of established control schemes to do so (*13*–*15*). A key advantage of achieving compliance in this way is that the robot can actively tune its compliance to best suit the task at hand without requiring any hardware modifications. However, implementing full actuation is burdensome for systems with many degrees of freedom. To be fully actuated, a robot must have as many actuators as degrees of freedom, but each additional actuator introduces extra cost, complexity, and mass into the system. Furthermore, to deploy any compliance control techniques on a robot arm requires it to have precise knowledge of its configuration and external contacts and to run its controller at a high enough frequency to react to external disturbances with an acceptable latency. Such a robot may also lose its compliance in the event of a controller failure, meaning that it only offers conditional safety.

Soft robots tend to achieve compliance via structure, which is more reliable because it is built into the robot itself. Soft robots (*16*, *17*), continuum robots (*18*, *19*), and series-elastic robots (*20*) that use actuators that permit multidirectional motion—such as McKibben muscles (*21*, *22*), bellows (*23*), fiber-reinforced elastomeric enclosures (FREEs) (*24*), and cable tendons (*25*)—are all examples of robots that are compliant because of their structure and/or material composition rather than feedback control. For this reason, we say such robots offer inherent safety. A disadvantage of this type of built-in compliance is its limited ability to be changed without making hardware modifications. For underactuated robots in particular, there does not necessarily exist a control input that can achieve a desired output compliance because of the passive compliance of the unactuated degrees of freedom. Even if a robot is capable of generating a desired force in a particular direction, its passive compliance in other directions may make it difficult to maintain its pose when an external load is applied. As a result, robot arms that exhibit structural compliance tend to substantially deform when external forces are applied, resulting in a limited payload capacity that makes them unsuitable for tasks in which compliance would be desirable but a larger payload is needed.

Previous research has sought to combine the advantages of structural compliance with the convenience and versatility of compliance via control. In rigid-bodied robots, this has been achieved by using variable stiffness actuators (VSAs) (*26*). VSAs actively modulate the stiffness of joints through lever arm mechanisms (*27*), antagonistic actuation schemes (*28*), and spring mechanisms (*29*). VSAs allow rigid-bodied robots to actively tune their built-in compliance during operation, enabling faster and safer motion control (*30*–*33*). In soft robots, which are inherently compliant, variable compliance is achieved through a number of active stiffening approaches that use jamming, shape-memory materials, temperature-dependent materials, and antagonistic actuation (*34*). This stiffening allows soft robots to increase the forces transferred to the environment when necessary.

John A. Paulson School of Engineering and Applied Sciences, Harvard University, 150 Western Ave., Boston, MA 02134, USA.
*Corresponding author. Email: dbruder@seas.harvard.edu

Although there are many examples of structures and actuators that enable robots to actively vary the compliance of their bodies, there is a need for principled modeling, design, and control approaches for effectively implementing variable compliance to achieve desired performance goals. Toward that aim, Stella *et al.* (*35*) presented a strategy for controlling the pose and physical stiffness of a soft robot arm to achieve a desired compliance at the point of contact with the environment. The approach was validated in simulation and on a real tendon-driven variable stiffness manipulator, enabling the robot to successfully perform a peg-insertion task. The work established a method for modeling and controlling the end-effector compliance of a soft robot arm but did not explore how such methods could be leveraged in design to overcome the current physical limitations of soft robots.

This paper presents a model-based design approach to effectively increase the payload capacity of soft underactuated robot arms. The proposed approach combines the advantages of structural compliance with the convenience and versatility of compliance via control. This approach does not require the arm to be fully actuated, reducing the complexity and cost per degree of freedom. It offers a paradigm for designing and constructing robot arms that exhibit inherent safety but with an increased payload capacity, making them well suited for myriad human-assistive tasks.

The contributions of this paper are threefold. First, through model-based analysis, we reveal how underactuated robot arms can use localized body stiffening to reduce the compliance at the end effector, resulting in an increased payload capacity. Second, we provide an experimental validation of the model and a demonstration of the advantages of localized body stiffening in both simulation and on a real robot arm (see Fig. 1). Third, we present a robot arm that achieves variable body stiffness using antagonistic actuation and demonstrate its usefulness in a real-world task that requires both compliance and strength.

RESULTS

Modeling

Compliance is a measure of the degree to which something resists deformation when a force is applied. For a given applied force, a material or structure with high compliance deforms more than a material or structure with low compliance. For many robotic applications, we are interested primarily in the compliance of the end effector, that is, the degree to which the end effector resists motion when an external force is applied to it. This "task-space compliance" is jointly determined by a robot's geometry, material composition, configuration, and control input. We desire a model that can describe this task-space compliance to reveal how to better design and control robot arms to support larger payloads.

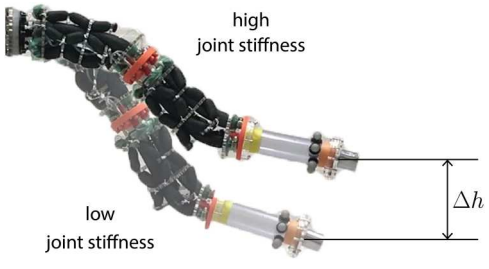

Fig. 1. Effect of joint stiffness on lifting. An underactuated robot arm sags under gravity because of the weight of its payload. However, this effect is substantially reduced by increasing the stiffness of some of its joints, which increases the height to which it can lift a payload by Δh.

There are a number of finite dimensional soft robot models, such as the piecewise-constant-curvature (*36*) and piecewise-smooth-curvature (*7*, *37*) models, cubic hermite splines models (*38*), pseudo-rigid body models (*39*–*41*), and many others (*42*). In this work, we chose to use a rigid-body model in which the arm is divided into a chain of rigid links connected by revolute joints, which has been shown to be sufficiently accurate to capture the behavior of real soft robots in navigation and manipulation tasks (*43*, *44*). This choice allows us to apply Cartesian impedance theory (*45*) to describe the relationship between configuration-space compliance and task-space compliance and readily gain useful insights regarding how to design more capable soft robot arms.

The following sections describe our modeling approach and its application to a planar robot arm. The model predictions suggest that compliance at the end effector can be substantially reduced by the localized stiffening of subsections of a robot arm without substantially reducing its range of motion. Within this modeling framework, robot configuration is described by a set of joint angles; therefore, we refer to the configuration space as joint space henceforth.

Joint-space compliance

A generic rigid-link arm consists of a series of N_{links} rigid links each of length ℓ_i connected by $N_{\text{joints}} = N_{\text{links}} - 1$ joints (see Fig. 2). The ith link has a coordinate frame fixed to it defined by the orthogonal set of unit vectors $\hat{x}_i, \hat{y}_i, \hat{z}_i$ where the origin is located at the base of the link and the $\hat{z}_i$ axis is pointing along the length of the link. Each joint can permit one, two, or three degrees of freedom. The displacement of the ith joint, $\mathbf{q}_i$, is thus described by up to three angles, α_i, β_i, γ_i, which describe the rotations about the $\hat{x}_i, \hat{y}_i, \hat{z}_i$ axes, respectively.

The configuration of the arm $\mathbf{q}$ can be described by the complete set of $n = 3(N_{\text{links}} - 1)$ joint angles

$$\mathbf{q} = \begin{bmatrix} \mathbf{q}_1 \\ \vdots \\ \mathbf{q}_{N_{\text{links}}-1} \end{bmatrix} = \begin{bmatrix} \alpha_1 & \beta_1 & \gamma_1 & \cdots & \alpha_{N_{\text{links}}-1} & \beta_{N_{\text{links}}-1} & \gamma_{N_{\text{links}}-1} \end{bmatrix}^\top \quad (1)$$

The arm is outfitted with N_{acts} actuators, with the input into the ith actuator denoted u_i. Such actuators could be electrically driven motors attached to the arm via tendons; fluid-driven actuators, such as bellows (*23*) and McKibben artificial muscles (*46*); or any other actuator that has nonzero compliance in the direction of actuation. These actuators can be affixed to the rigid-bodied spine in many ways. They may exert joint torques directly [for example, the "Grub" robot in (*47*)], they may be aligned parallel to the spine to indirectly induce joint torques and bending (*48*–*51*), or they may be coupled in some other way. For our purposes, we assume only that the potential energy stored in the ith actuator can be described as a function of the arm configuration and input, that is, $U_i^{\text{act}}(\mathbf{q}, u_i) \in \mathbb{R}$. This assumption will allow us to express the joint torques as a function of the joint angles $\mathbf{q}$ and actuator inputs $\mathbf{u} = [u_1, \cdots, u_{N_{\text{acts}}}]^\top$.

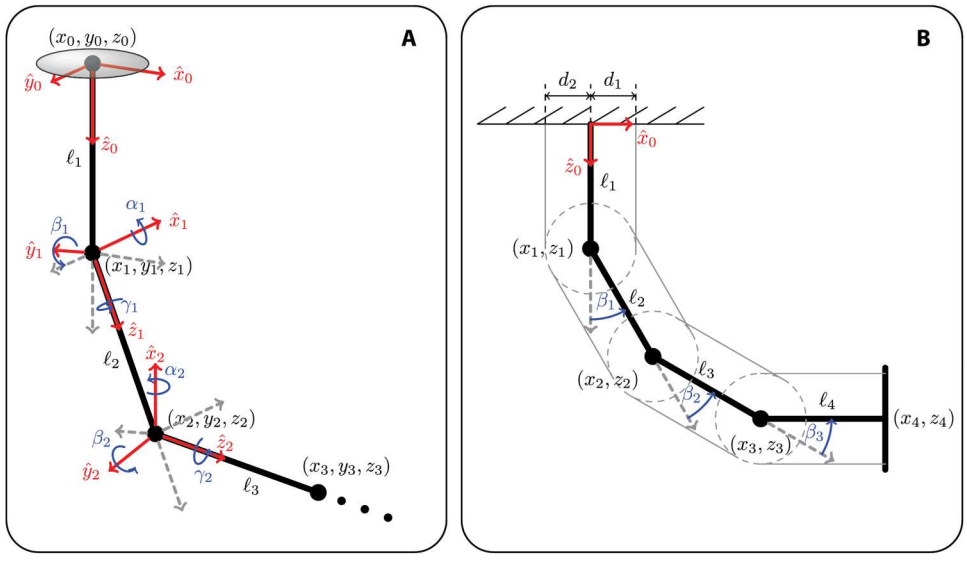

Fig. 2. Generic robot arms. (**A**) A generic robot arm consisting of a series of rigid links connected by joints with three degrees of freedom. The orientation of a link relative to its predecessor is described by a set of three joint angles. (**B**) An example planar robot arm where each joint has just one degree of freedom.

We can derive an expression for the joint torques as a function of the configuration and actuator inputs using the principle of the conservation of energy. The total potential energy of the arm, U, can be expressed as the sum of the potential energy stored in the actuators and body

$$U(\mathbf{q}, \mathbf{u}) = U^{\text{act}}(\mathbf{q}, \mathbf{u}) + U^{\text{body}}(\mathbf{q}) \tag{2}$$

where $U^{\text{act}}(\mathbf{q}, \mathbf{u})$is the sum of all of the actuator energies and $U^{\text{body}}(\mathbf{q})$ is the total potential energy stored in the robot body, including the elastic energy stored in the joints and the gravitational potential energy due to the mass of the links. The principle of conservation of energy implies that for a virtual displacement of the system from static equilibrium, $\delta\mathbf{q}$, the sum of the work of the joint torques, $\boldsymbol{\tau}_q$, and the change in potential energy are equal to zero, that is

$$\boldsymbol{\tau}_q^\top \delta\mathbf{q} + \delta U = 0 \tag{3}$$

We can apply the chain rule to express the change in total potential energy in terms of the virtual displacement

$$\delta U = \frac{\partial U(\mathbf{q}, \mathbf{u})}{\partial \mathbf{q}} \delta\mathbf{q} \tag{4}$$

Equation 4 can be substituted into Eq. 3, and because it holds for any virtual displacement $\delta\mathbf{q}$, Eq. 3 can then be simplified to yield the following expression for the joint torques

$$\boldsymbol{\tau}_q(\mathbf{q}, \mathbf{u}) = -\frac{\partial U(\mathbf{q}, \mathbf{u})}{\partial \mathbf{q}}^\top \tag{5}$$

For a given configuration $\mathbf{q}$ and input $\mathbf{u}$, we assume the joint stiffness induced by the actuators to be locally linear. That is, for some stiffness matrix $K_q \in \mathbb{R}^{n \times n}$, the following relationship holds in a neighborhood of $\mathbf{q}$

$$\delta\boldsymbol{\tau}_q = K_q(\mathbf{q}, \mathbf{u})\delta\mathbf{q} \tag{6}$$

where $\delta\boldsymbol{\tau}_q$ is the resulting change in joint torques due to the displacement. This stiffness matrix encodes the local change in joint torques given a joint displacement. Hence, it can be defined as the partial derivative of $\boldsymbol{\tau}_q$ with respect to $\mathbf{q}$, which is equivalent to the negative second partial derivative of the total potential energy U with respect to $\mathbf{q}$

$$K_q(\mathbf{q}, \mathbf{u}) = \frac{\partial \boldsymbol{\tau}_q(\mathbf{q}, \mathbf{u})}{\partial \mathbf{q}} = -\frac{\partial^2 U(\mathbf{q}, \mathbf{u})}{\partial \mathbf{q}^2} \tag{7}$$

The joint compliance matrix $C_q \in \mathbb{R}^{n \times n}$ encodes the local joint displacement given a set of applied joint torques. It satisfies the inverse relationship to Eq. 6

$$\delta\mathbf{q} = C_q(\mathbf{q}, \mathbf{u})\delta\boldsymbol{\tau}_q \tag{8}$$

Hence, it is defined as the inverse of the stiffness matrix

$$C_q(\mathbf{q}, \mathbf{u}) = K_q^{-1}(\mathbf{q}, \mathbf{u}) \tag{9}$$

This inverse exists as long as no joints have zero stiffness, which we assume to be the case for any robot arm that approximates the behavior of a continuum arm.

Task-space compliance

Let the Cartesian coordinates of the end of each link of our arm be described by the vector $\mathbf{x} \in \mathbb{R}^{3N_{\text{links}}}$ defined as

$$\mathbf{x} = \begin{bmatrix} x_1 & y_1 & z_1 & \cdots & x_{N_{\text{links}}} & y_{N_{\text{links}}} & z_{N_{\text{links}}} \end{bmatrix}^\top \tag{10}$$

We say that $\mathbf{x}$ describes the configuration of the robot in task space, whereas $\mathbf{q}$ describes it in joint space.

The relationship between displacement and force is captured by the robot's task-space compliance C_x, which satisfies the following relation

$$\delta\mathbf{x} = C_x(\mathbf{q}, \mathbf{u})\delta\boldsymbol{\tau}_{x,\text{ext}} \tag{11}$$

where $\delta\boldsymbol{\tau}_{x,\text{ ext}}$ is an externally applied virtual force and $\delta\mathbf{x}$ is the resulting virtual displacement. This task-space compliance matrix is related to the joint-space compliance matrix via the following

equation

$$C_x(\mathbf{q},\mathbf{u}) = J_x(\mathbf{q})C_q(\mathbf{q},\mathbf{u})J_x^\top(\mathbf{q}) \tag{12}$$

where $J_x(\mathbf{q}) = \frac{\partial \mathbf{x}}{\partial \mathbf{u}}$ is the standard manipulator Jacobian (*52*). The Supplementary Materials contain a complete derivation of Eq. 12 and Algorithm 1, which summarizes the steps to compute the task-space compliance matrix given $\mathbf{q}$ and $\mathbf{u}$.

The task-space stiffness matrix, K_x, is defined as the inverse of the task-space compliance matrix, that is, $K_x(\mathbf{q}, \mathbf{u}) = C_x(\mathbf{q}, \mathbf{u})^{-1}$. Note that this inverse is only well defined when the arm is not at a kinematic singularity (for example, completely straight), because in such cases the manipulator Jacobian J_x ceases to be full rank. For example, when an arm is in a completely straight configuration, it has zero task-space compliance along the direction the arm is pointing. The inverse of 0 is not well defined; therefore, neither is the corresponding task-space stiffness in this direction. The compliance matrix is well defined even at kinematic singularities, however. For this reason, it is more convenient to describe the robot's resistance to deformation in task space in terms of compliance rather than stiffness.

Example: Planar arm driven by McKibben muscles

To illustrate the relationship between joint compliance and task-space compliance, we consider an example system consisting of an articulated planar arm outfitted with McKibben muscles to provide actuation. This section walks through the derivation of the compliance matrix for this system and shows how the model reveals a way to increase the arm's payload capacity through localized body stiffening.

For this example, we consider a massless planar four-link robot arm ($N_{\text{links}} = 4$, $N_{\text{joints}} = 3$), where every link has a length of 0.25 m, that is, $\ell_i = 0.25\text{m}\ \forall\ i = 1, \ldots, N_{\text{links}}$, shown in Fig. 2B. In this planar example, the displacement at the i^{th} joint is described by a single-joint angle β_i about the y axis. The configuration of the arm in joint space is thus given by the $N_{\text{joints}} \times 1$ vector

$$\mathbf{q} = \begin{bmatrix} \beta_1 & \cdots & \beta_{N_{\text{joints}}} \end{bmatrix}^\top \tag{13}$$

and the configuration of the arm in task space is given by the $2N_{\text{links}} \times 1$ vector

$$\mathbf{x} = \begin{bmatrix} x_1 & z_1 & \cdots & x_{N_{\text{links}}} & z_{N_{\text{links}}} \end{bmatrix}^\top \tag{14}$$

Each joint has a passive stiffness denoted $k_i = -0.5$ Nm that contributes a displacement-dependent joint torque according to Hooke's law, that is, $\tau_{\beta_i} = k_i\beta_i$.

The arm is actuated by two McKibben artificial muscles ($N_{\text{acts}} = 2$) mounted to opposite sides. They are spaced a distance of 0.1 m from the arm's centerline, which is captured by the vector of actuator offsets, $\mathbf{d} = [-0.1, 0.1]^\top$m. The two McKibben muscles have identical parameters (*53*); the length of the fibers of their braided sleeves is $B_f = 1.4$ m, and the number of revolutions the fibers make from one end to the other is $N_f = 1$. The control input $\mathbf{u}$ is defined as the vector of fluid pressures inside the McKibben muscles, that is, $\mathbf{u} = [p_1, p_2]^\top$.

The derivation of the task-space compliance matrix, $C_x(\mathbf{q}, \mathbf{u})$, for this example arm is included in the Supplementary Materials. We can visualize the arm's end-effector compliance by computing the resulting displacements from a set of unit forces applied to the end effector. Doing so for all forces in the unit sphere generates the compliance ellipsoid

$$\begin{aligned} \mathscr{C}(\mathbf{q},\mathbf{u}) = \{&\delta\mathbf{x} = C_x(\mathbf{q},\mathbf{u})\boldsymbol{\tau}_{\text{ext}} \\ &\text{such that } \|\boldsymbol{\tau}_{\text{ext}}\| = 1 \\ &\boldsymbol{\tau}_{\text{ext},i} = 0 \text{ for } i = 1, \ldots, 2(N_{\text{joints}} - 1)\} \end{aligned} \tag{15}$$

Because the arm is planar in this case, we only consider forces in the xz plane, resulting in a compliance ellipse.

Figure 3 illustrates how changing the joint stiffnesses affects the compliance at the end effector. Figure 3A shows the equilibrium configuration and compliance ellipse for the arm given a control input of $\mathbf{u} = [1, 50]^\top$ Pa with a passive stiffness of 0.05 Nm at every joint. Figure 3C shows the equilibrium configuration and compliance ellipse given the same input but with an increased stiffness of 5 Nm at every joint. As expected, the size of the compliance ellipsoid decreased as the joint stiffnesses increased. However, it should also be noted how the equilibrium position moves closer to the origin, indicating a reduction in the arm's range of motion. There is thus a trade-off between end-effector compliance and the size of the workspace.

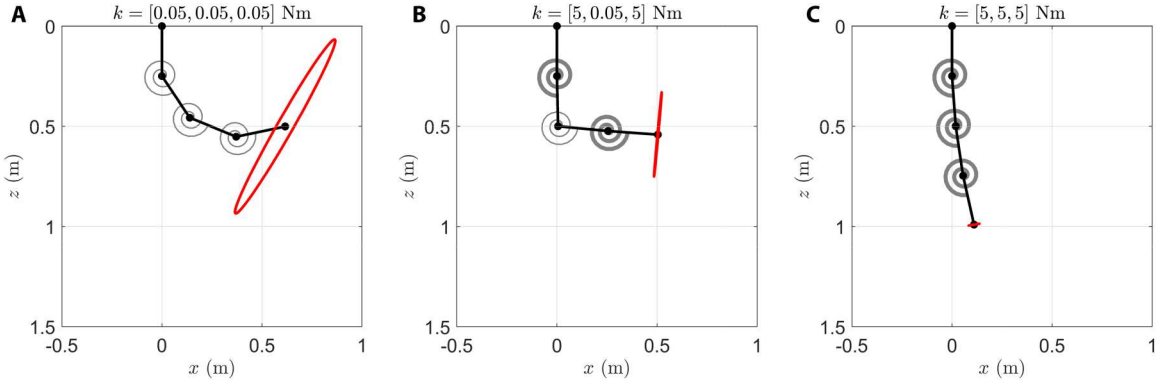

Fig. 3. Compliance ellipse for various joint stiffnesses. The equilibrium position and compliance ellipse of a planar arm driven by two McKibben muscles pressurized to 1 and 50 Pa according to the model. In (**A**), all joints have low stiffness, so it shows substantial deformation and a large compliance ellipse. In (**C**), all joints have high stiffness, so it shows little deformation and a small compliance ellipse. In (**B**), joints 1 and 3 have high stiffness, allowing the arm to show substantial deformation while also reducing the size of the compliance ellipse. Note that thicker springs denote higher stiffness at each joint.

It is possible to sidestep this trade-off, however, as illustrated by Fig. 3B. By increasing the stiffness of just a subset of the joints rather than all of them, the compliance of this arm can be reduced without substantially reducing its range of motion. Figure 3B shows the equilibrium configuration and compliance ellipsoid for the arm given the same control input but with an increased stiffness of 5 Nm at joints 1 and 3 only. Compared with Fig. 3A, the size of the compliance ellipsoid is substantially reduced, but the height of the end effector remains nearly unchanged. In the following sections, we validate this behavior in both simulation and on a real system and demonstrate how this principle can be exploited to increase the strength and functionality of soft robotic systems through localized body stiffening.

Evaluation

The model presented in the previous section predicts that by stiffening a subset of its joints, an underactuated robot arm can substantially reduce its end-effector compliance without sacrificing its range of motion. We validated these predictions in both simulation and on a real system.

We leveraged the PyBullet physics engine (*54*) and the SoMo (*43*) and SoMoGym (*44*) frameworks to construct and simulate a dynamically realistic planar manipulator arm. The arm is composed of two bending sections or "modules" made up of 17 links connected by 16 joints with customizable stiffnesses and a longer rigid segment connected to its end effector to extend its range of motion. This simulated robot arm enables us to observe the effect of stiffening many different subsets of joints without having to physically implement such behavior.

The real robot arm that we constructed consists of two pneumatically actuated segments, each with a spine made up of four compliant universal joints, and a third rigid segment meant to extend its range of motion (see Fig. 4). Each segment is equipped with the ability to stiffen three of four of its joints using an antagonistic actuation scheme. The stiffnesses of the joints spanned by antagonistic pneumatic actuators are proportional to the antagonistic actuation pressure, denoted p_a. This design enables us to observe the effect of modulating the stiffness of this particular subset of joints and to showcase how this ability is useful in a real robotic system. Further details on the simulated and real robot arm implementations can be found in the Materials and Methods.

The following subsections describe the experiments that we conducted to validate the insights provided by our model on both the simulated and the real robot arms. Experiment 1 measured the compliance ellipse of both robot arms. Experiment 2 measured the range of motion of both robot arms over a set of different payloads. Experiment 3 demonstrated the benefit of our implementation of adjustable compliance for a manipulation task in a cluttered environment.

Experiment 1: Characterization of compliance/stiffness

Compliance ellipse of simulated robot

The compliance ellipse as defined in (*15*) is the set of displacements resulting from applying forces in the unit circle to the end effector. We approximated the compliance ellipse by sampling over a set of 32 applied end-effector forces and recording the corresponding displacement for each one. Starting from its equilibrium position given an actuation torque of 1 Nm applied at every joint, we applied the following set of forces (in N) to the simulated arm's end effector

$$\mathcal{F}_{\text{comp}} = \left| \left\{ \begin{bmatrix} \frac{1}{2}\cos\theta \\ 0 \\ \frac{1}{2}\sin\theta \end{bmatrix}^{\top} \;\middle|\; \theta = \frac{\pi}{32} n \text{ for } n = 0, 1, 2, \ldots, 32 \right\} \right. \quad (16)$$

and recorded its position after it settled into its new equilibrium.

The compliance ellipse was measured for 12 different joint stiffness conditions. In each trial, the stiffness of a subset of 4, 14, or 15

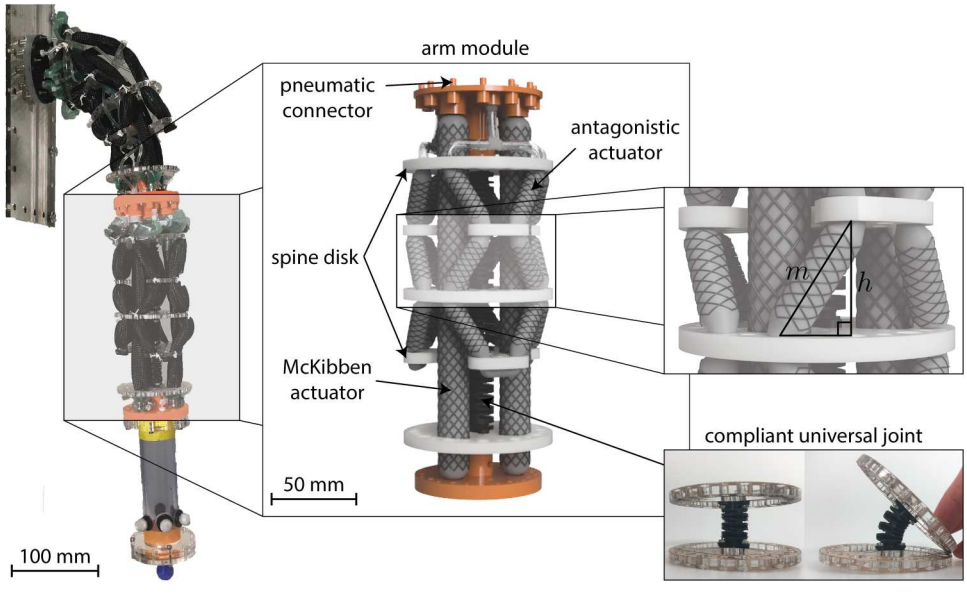

Fig. 4. Schematic of soft robot arm. The soft robot arm used in our experiments consists of two modules connected by a custom 3D-printed pneumatic connector. The arm's spine consists of compliant universal joints made up of a series of flexures. Each flexure has a small range of motion, but, in series, they permit deformations of up to 90°. McKibben actuators oriented parallel to the spine induced bending deformations, whereas a second set arranged in a truss structure induced joint stiffening through antagonistic actuation.

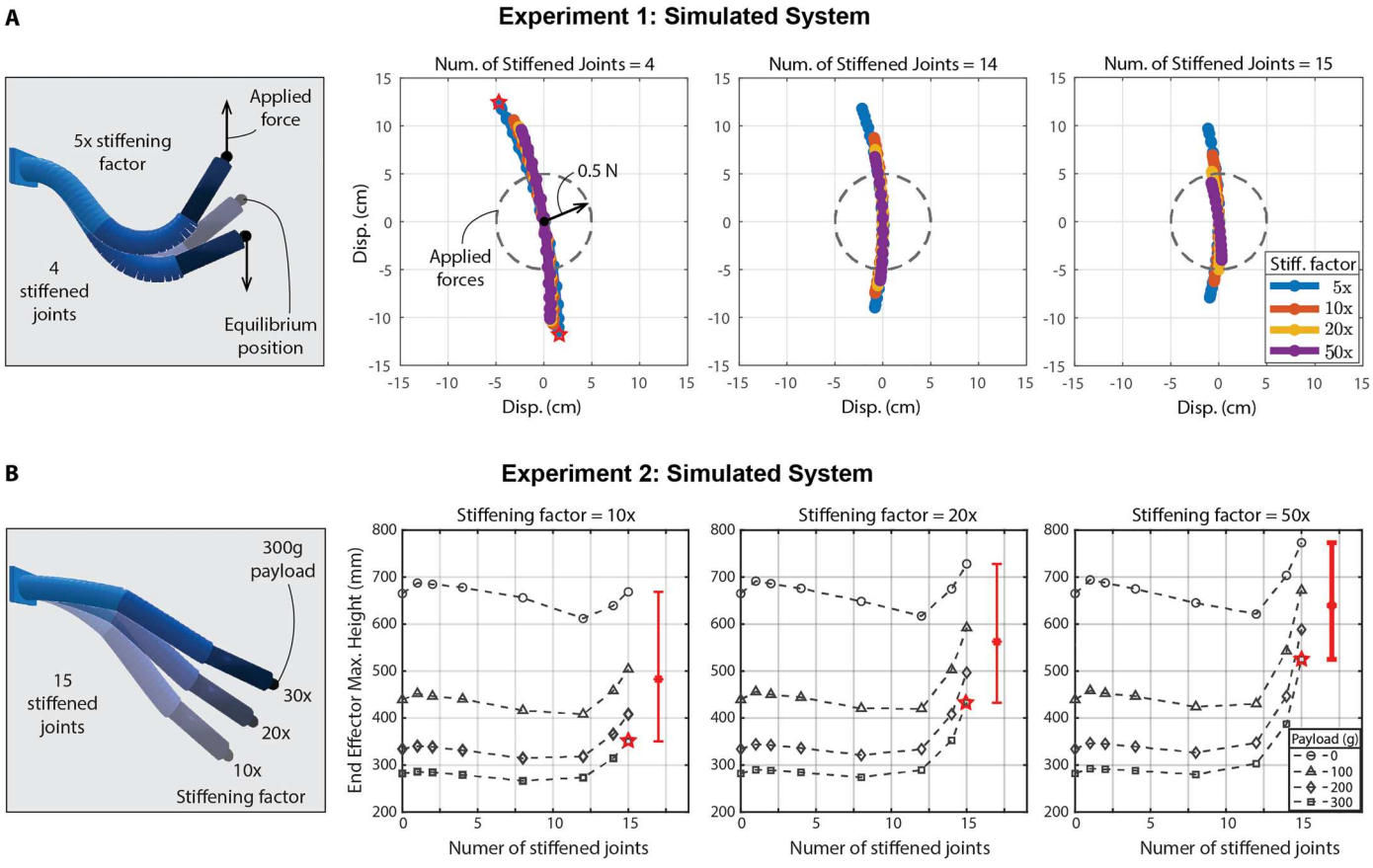

Fig. 5. Simulation experiment results. (**A**) Starting from its equilibrium position, a set of 32 forces sampled from a circle of radius 0.5 N are applied to the simulated arm's end effector (just two shown in left image). The resulting set of displacements form the compliance "ellipse." As the stiffnesses of some joints were increased, the compliance ellipse shrank. This effect became more pronounced as more joints were stiffened. (**B**) The maximum end-effector height was recorded given a constant torque of 1 Nm applied to all joints. The height depends on the number of stiffened joints and the magnitude of their stiffness. The red bar highlights the range of end-effector heights over all payloads for 30 (of 32) stiffened joints, and the mean is indicated by an asterisk. As the stiffness magnitude increased, so did the mean end-effector height. Red stars indicate data points that correspond to the configurations shown in the images on the left.

joints per module was multiplied by a "stiffening factor" of 5, 10, 20, or 50. The particular joints included in the subsets of 4, 14, and 15 joints are specified in table S1, visualizations of the compliance ellipses for these cases are displayed in Fig. 5, and a video showing how the compliance ellipse was measured for the case when four joints per module were stiffened by a factor of 50 is included in the Supplementary Materials as movie S1.

Stiffness ellipse of real robot

In practice, it is difficult to apply unit forces to the end effector of a real robot because this requires feedback control around a force setpoint. Therefore, rather than measuring the compliance ellipse directly, we characterized compliance by measuring its inverse, the stiffness ellipse, which consists of the set of reaction forces resulting from end-effector displacements in the unit circle.

The end effector of the real soft robot arm was affixed to the end effector of a commercial UR5 robot arm via a three-dimensional (3D) printed ball-and-socket joint that constrained its position without constraining its orientation. The end effector of the UR5 traced out a circle in the *xz* plane with a diameter of 12 cm, while a six-axis load cell mounted to the UR5 end effector recorded the reaction forces imposed by the soft robot arm (see Fig. 6).

This procedure was repeated four times. In all four trials, the soft robot actuator pressures were equal to zero, but the antagonistic actuator pressures responsible for modulating joint stiffnesses were 0, 69, 138, and 207 kPa. A video showing all four trials is included in the Supplementary Materials as movie S2.

Experiment 2: Characterization of range of motion

The functional benefit of increasing the end effector stiffness of a robot arm is the extent to which it increases the arm's payload capacity. We validated this benefit experimentally by characterizing the range of motion of our simulated and real robot arms for several payloads while varying their joint stiffnesses.

Range of motion of simulated robot

Given a constant applied torque of 1 Nm to each of its joints, we recorded the steady-state height of the simulated robot arm's end effector over a collection of 96 different joint stiffness and loading conditions. In each trial, the stiffnesses of a subset of joints were multiplied by a stiffening factor of 10, 20, or 50, and the end-effector payload was set to 0, 100, 200, or 300 g. The complete list of joint subsets is provided in table S1, and the results of the experiment are displayed in Fig. 5. It was not feasible to include video footage of all trials, so a video showing just the trials with subsets of 0, 4, 14, and

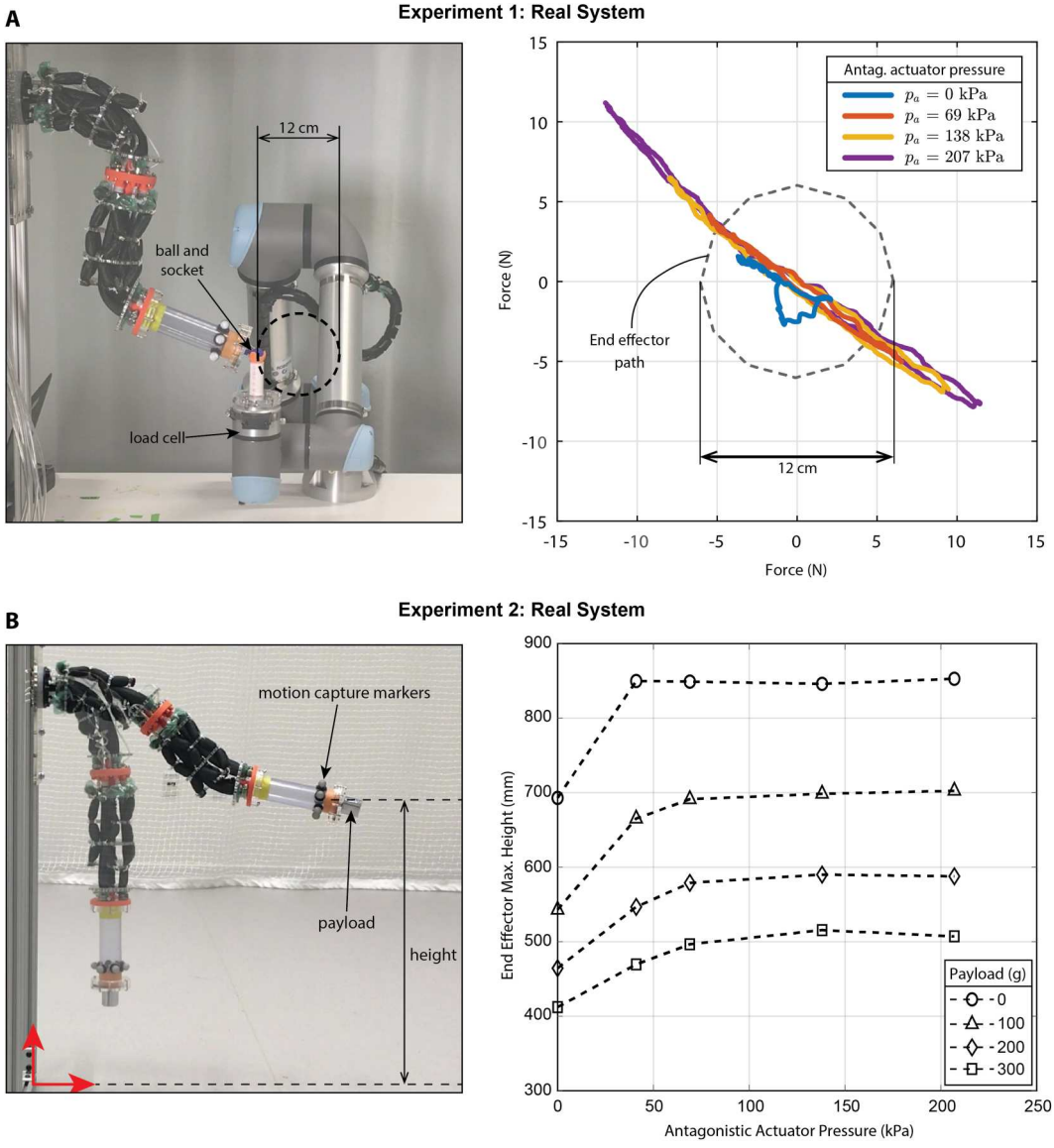

Fig. 6. Real experiment results. (**A**) A load cell mounted to the end effector of a UR5 robot measured reaction forces while the soft robot arm's end effector traced out a circular trajectory. The stiffness ellipse is the set of reaction forces corresponding to displacements along the circlular trajectory. As the pressure in the antagonistic actuators increased, so did the size of the stiffness ellipse. (**B**) A motion capture system records the position of the end effector under a lifting input sequence (*17*) for several payloads. As the antagonistic actuation pressure increased, so did the maximum height of the end effector.

15 stiffened joints per module given a stiffening factor of 50 and a 200 g of payload is included in the Supplementary Materials as movie S3.

Range of motion of real robot

For the real robot case, we again consider motions only in the *xz* plane and command an actuator pressure trajectory to produce a simple 30-s lifting motion

$$\mathbf{u}(t) = \begin{cases} [0, 20.7t, 20.7t, 0, 20.7t, 0]^\top & 0 \le t < 10 \\ [0, 207, 207, 0, 207, 0]^\top & 10 \le t < 15 \\ [0, -20.7t, -20.7t, 0, -20.7t, 0]^\top & 15 \le t < 25 \end{cases} \quad (17)$$

where the *i*th component of **u** specifies the pressure in the *i*th actuator in kPa. We tracked the position of the end effector throughout the trajectory using a Vicon motion capture system (see Fig. 6) and repeated for every combination of antagonistic actuator pressures in the set {0,41,69,138,207} kPa and payloads in the set {0,100,200,300} g (see Fig. 6). A video showing the trials for a 0 g of payload and a 300 g of payload is included in the Supplementary Materials as movie S4.

Experiment 3: Demonstration of the benefit of tunable compliance

A robot arm with the ability to vary its joint stiffnesses is well suited for real-world tasks that require a combination of compliance and strength to successfully complete. This includes a broad class of tasks that involve navigating in an obstacle-rich environment and applying force to the environment at the end effector. Example

applications include duct and pipe cleaning, search and rescue in disaster sites, and robotic laparoscopic surgery.

To simulate the demands of this type of application, we assigned our real robot arm the task of toggling a switch located within an obstacle-filled environment. This task requires enough flexibility to adapt to the geometry of the obstacles and enough strength to overcome the resistance of the switch. A peg board with 12 pegs arranged as shown in Fig. 7 was used as a stand-in for a generic cluttered environment along with a custom-made switch with a toggling force threshold of 7 N.

At the beginning of the experiment, the stiffening pressure was set to $p_a = 0$ kPa; that is, extra stiffness was not being added to any of the joints. As the arm approached the peg board, it bent to navigate the geometry of the environment. The robot lacked the sensing and dexterity needed to completely avoid the pegs, so it relied on its compliance to adapt its shape to accommodate the pegs. Eventually, the end effector reached the switch but was not capable of exerting the necessary force to toggle the switch. To remedy this, p_a was set to 207 kPa, which had the effect of reducing the arm's end-effector compliance such that it overcame the 7-N switch toggling threshold. A video of this demonstration is included in the Supplementary Materials as movie S5.

DISCUSSION

The results of experiment 1 demonstrate how increasing joint stiffnesses affects the task-space compliance at the end effector. According to our model, increasing joint stiffnesses should reduce the task-space compliance at the end effector, and this effect should become more pronounced as more joints are stiffened. The compliance ellipse of the simulated robot arm confirms this relationship. Figure 5 shows that for a given subset of joints, increasing their stiffness reduces the size of the compliance ellipse, and this effect is substantially more pronounced when 15 joints are stiffened rather than just four.The stiffness ellipse of the real robot arm also confirms the relationship between joint stiffnesses and task-space compliance predicted by our model. Figure 6 shows that as the stiffnesses of the joints spanned by antagonistic actuators increased, so did the size of the stiffness ellipse, indicating an increase in the task-space stiffness measured at the end effector.

The measured compliance and stiffness "ellipses" do not actually take on elliptical shapes. This is because an ellipse represents a local linearization of the end-effector compliance; outside of a local neighborhood of an equilibrium point, the end-effector compliance is nonlinear. In our experiments, the end-effector displacement was large enough to observe this nonlinear behavior.

The flattened shape of the ellipses also illustrates how the stiffness is much greater in the direction perpendicular to the length of the final link than in the direction parallel to it. This highlights one potential limitation of modifying task-space compliance by stiffening groups of joints rather than controlling their stiffnesses individually. Although the desired decrease in task-space compliance is achieved along the major axis of the stiffness ellipse, there is little noticeable difference in the compliance in all other directions. Modifying the compliance in specific directions would require full actuation or the ability to stiffen joints individually. This ability would come at a cost, however, because both of these options introduce greater complexity into the system.

The results of experiment 2 demonstrate the effect that increasing joint stiffnesses has on a robot's workspace. As predicted by the model and shown in Fig. 3, increasing the stiffness of all joints reduces a robot's range of motion, but increasing a subset of joints while leaving the stiffness of some unchanged allows the robot to maintain a large range of motion while decreasing its task-space compliance. As a result, the arm can lift larger payloads when a subset of its joints are stiffened than when none or all of its joints are stiffened.

For a given constant torque applied at all joints, increasing the joint stiffnesses of the simulated robot arm increased the end-effector height for each payload and made the height more consistent across payloads. As seen in Fig. 5, for a given stiffening factor and payload, the end-effector height was largest when all but two joints were stiffened. Averaged across all payloads, the end-effector height was 9, 17, and 25% greater than those achieved without any joints stiffened for stiffening factors of 10, 20, and 50, respectively. Furthermore, increasing the stiffening factor reduced the range of observed end-effector heights across payloads, exhibiting greater consistency with respect to loading. This effect is consistent with a decrease in the end-effector compliance caused by increased stiffening of select joints, just as observed in experiment 1.

Similar results were observed using the real robot arm. For every payload, increasing the joint stiffnesses resulted in an increase in the maximum height of the end effector of 20 to 30%. Although the real arm was unable to modify the subset of joints that would be stiffened, the magnitude of the stiffness could be adjusted by modulating the pressure of the antagonistic actuators. Notably, increasing the pressure beyond 69 kPa had little effect in the arm's behavior, as seen in Fig. 6. This indicates that the stiffness induced by 69 kPa

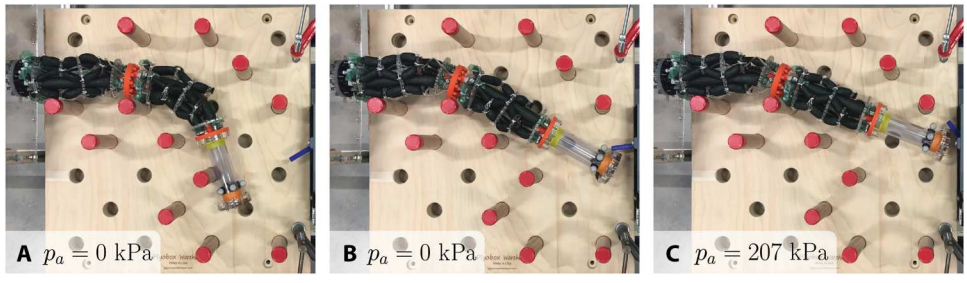

Fig. 7. Switch toggling task in cluttered environment. (**A**) The soft robot exploited its compliance to navigate around peg obstacles via contact, (**B**) but it was unable to toggle a switch because of its large end-effector compliance. (**C**) After reducing its end-effector compliance by increasing joint stiffnesses, the arm was able to successfully toggle the switch.

approximated the behavior of completely immobilized joints well enough that further increases in pressure were unnecessary.

Experiment 3 highlights the utility of adjustable compliance in a robot arm. A highly compliant system that can adapt to irregular geometries is well suited for navigation through a cluttered environment, but toggling a switch with a nontrivial force threshold is more easily achieved with a rigid arm with low end-effector compliance. Thus, performing this task would be challenging, or outright infeasible, with a fully-soft underactuated arm or a rigid fully actuated arm. However, because our robot arm had the capability to actively tune its compliance, it was able to successfully execute both parts of the task.

Our hardware experiments demonstrate the practical benefit of adjustable compliance and the feasibility of implementing this capability via antagonistic actuation. This design approach could lead to much more capable soft robot arms in the future by increasing their payload capacity without sacrificing their ability to use compliance to navigate in obstacle-rich environments and to safely interact with humans and delicate objects. Furthermore, improvements on this design that allow for tuning the stiffnesses of individual joints rather than just large groups of joints would enable control of both the size and the orientation of the compliance ellipsoid for tasks that demand larger compliance in certain directions than others. The arm′s performance could also be improved by reducing its weight to mitigate the effect of self-loading. This could be achieved by using lighter materials or by tapering the arm diameter and mass along its length. In addition, pneumatic actuation is not practical for all applications, so alternative actuation and stiffening technologies could be explored, such as dielectric elastomer actuators (*55*, *56*), twisted string actuators (*57*, *58*), and cable-driven approaches (*35*, *59*).

In this paper, we presented a modeling approach for soft underactuated robot arms that describes the relationship between actuation pressures, force, joint stiffnesses, and end effector compliance. We used this model to show how it is possible to increase their payload capacity just by tuning the stiffnesses of a subset of joints. We verified these model predictions in simulation and on a real robot arm and demonstrated a way to actively modulate joint stiffnesses in hardware through antagonistic actuation. Future work should explore other methods of active joint stiffening and task-specific control of joint stiffnesses to further improve the performance of soft and underactuated robots.

MATERIALS AND METHODS

Simulated arm design

We constructed a planar robot arm in simulation to validate the insights of the analytical model described in Results. This simulated arm allowed us to individually vary the stiffness of each joint for an arm with a large number of short rigid links per actuator, which would be difficult to achieve with a physical robot. The arm was implemented using the SoMoGym (*44*) and SoMo (*43*) frameworks, which rely on the PyBullet physics simulator (*54*) to achieve dynamically realistic simulations.

The arm consists of two individually controlled segments with a length of 240 mm and a mass of 300 g connected in series. Each segment consists of a chain of 17 links connected by 16 joints with passive stiffnesses of 300 Nm. A rigid end effector with a length of 160 mm and a mass of 200 g was mounted to the distal end of the second actuated segment.

Real arm design

To validate the relationship between joint-space compliance, task-space compliance, and payload capacity predicted by our model and exhibited in simulation, we constructed a real robot arm with the ability to markedly increase the stiffness of a subset of its joints using an antagonistic actuation scheme.

Similar to the simulated arm, the real arm consisted of two individually controlled segments with a length of 240 mm connected in series. Each segment consisted of a chain of compliant joints that comprised a central "spine" and was actuated by three McKibben muscles spaced evenly around the spine at a radius of 22 mm. A second set of McKibben muscles was arranged in a radially symmetrical "truss structure" (see Fig. 4). When actuated, these McKibben muscles compressed the spine and pulled against one another, increasing the stiffness of the joints they surround. Essentially, the spine and truss actuators together formed a tensegrity structure that then approached the behavior of a single rigid link as the pressure in the truss actuators increased.

A rigid end effector composed of a 160-mm-long clear polyvinyl chloride pipe with a mass of 200 g was mounted to the distal end of the second actuated segment. Such a long end effector was chosen to amplify small changes in orientation of the distal end of the second actuated segment by converting them to larger changes in displacement. This served to increase the robot′s workspace and make the effect of stiffening its joints easier to observe. The following subsections highlight several of the key features of this design and describe them in more detail.

Compliant universal joints

Our spine consisted of a chain of compliant flexure-based universal joints that permit motion about the x and y axes while resisting motion about the z axis (see Fig. 4). Each universal joint consisted of a series of four alternating flexures about the x and y axes, respectively. Although each flexure has a small range of motion (15° to 25°), collectively they enable deformations up to 90°. The joints were 3D printed on a Prusa MK3S+ out of FilaFlexible40 filament, a thermoplastic with hardness 40D.

Spine stiffening through antagonistic actuation

Antagonistic actuation consists of two or more actuators acting on a joint in such a way that in a given configuration, the net joint torque cancels out to zero. The configuration of the joint remains unchanged, but its stiffness increases because any externally applied force must work against one or more of the actuators to induce motion at the joint. Animals and humans often use antagonistic actuation to control the stiffness of their joints (*60*), and the approach has commonly been adopted in soft robotic systems as well (*61*–*63*)].

We used McKibben muscles to provide antagonistic actuation and increase the stiffness of a subset of the robot arm′s joints. McKibben actuators have a limited range of motion, typically displaying contraction ratios of only 20 to 30% (*21*, *53*); thus, they impose restrictions on a joint′s range of motion when coupled together. We desired the McKibben actuators to be arranged so that they induce stiffening when active but exert minimal restrictions on the motion of joints when they are inactive. To that end, they were

symmetrically arranged in a truss pattern around the spine (see Fig. 4). Arranging them in a truss pattern rather than parallel to the arm's spine enabled larger joint deformations for a given change in McKibben length.

This can be seen by considering one section of the truss pattern, which is a right triangle with height h equal to the distance between spine disks and hypotenuse m equal to the length of McKibben spanning it (see Fig. 4). It follows from differentiating the pythagorean theorem with respect to h that a virtual change in the height of δh corresponds to a virtual change in the hypotenuse of only $\delta m = \frac{h}{m}\delta h < \delta h$. This means that the distance between spine disks can change more than the length of the McKibben changes. As a consequence, the joints have a larger range of motion than they would if the McKibben actuators were arranged parallel to the spine (in such a case, $\delta m = \delta h$). An additional benefit of the truss arrangement is that it provides antagonistic stiffening in the roll, pitch, and yaw axes rather than just the roll and pitch axes.

Fabrication of actuators and connectors

Each McKibben muscle actuator was composed of an airtight bladder made from a sheet of thermoplastic polyurethane (Stretchlon 200 bagging film) wrapped in polyester fray–resistant expandable sleeving. The internal McKibben actuators used sleeving with an inner diameter of 19 mm (McMaster-Carr, item no. 2837 K75), and the antagonistic Mckibben actuators used sleeving with an inner diameter of 13 mm (McMaster-Carr, item no. 2837 K74). The ends of the McKibbens were secured using worm-drive hose clamps (McMaster-Carr, item no. 5011 T141).

The spine disks were laser-cut from an acrylic sheet with a thickness of 6 mm, and the pneumatic connectors between modules were 3D printed out of polylactic acid using a Prusa MK3S+. Computer-aided design files for the spine disks and pneumatic connectors can be accessed using the following DOI: 10.5281/zenodo.8256878.

Supplementary Materials

This PDF file includes:
Methods
Table S1

Other Supplementary Material for this manuscript includes the following:
Movies S1 to S5
Data file S1

REFERENCES AND NOTES

1. A. Zlatintsi, A. C. Dometios, N. Kardaris, I. Rodomagoulakis, P. Koutras, X. Papageorgiou, P. Maragos, C. S. Tzafestas, P. Vartholomeos, K. Hauer, C. Werner, R. Annicchiarico, M. G. Lombardi, F. Adriano, T. Asfour, A. M. Sabatini, C. Laschi, M. Cianchetti, A. Güler, I. Kokkinos, B. Klein, R. López, I-Support: A robotic platform of an assistive bathing robot for the elderly population. *Rob. Auton. Syst.* **126**, 103451 (2020).
2. M. Manti, A. Pratesi, E. Falotico, M. Cianchetti, C. Laschi, Soft assistive robot for personal care of elderly people, in *2016 6th IEEE International Conference on Biomedical Robotics and Biomechatronics (BioRob)* (IEEE, 2016), pp. 833–838.
3. D. P. Miller, Progress on the deictically controlled, in *Assistive Technology and Artificial Intelligence* (Springer, 1998), pp. 126–136.
4. B. T. Phillips, Deep-sea hydrothermal vents as natural egg-case incubators at the Galapagos Rift. *Sci. Rep.* **8**, 1788 (2018).
5. N. R. Sinatra, C. B. Teeple, D. M. Vogt, K. K. Parker, D. F. Gruber, R. J. Wood, Ultragentle manipulation of delicate structures using a soft robotic gripper. *Sci. Robot.* **4**, eaax5425 (2019).
6. K. C. Galloway, K. P. Becker, B. Phillips, J. Kirby, S. Licht, D. Tchernov, R. J. Wood, D. F. Gruber, Soft robotic grippers for biological sampling on deep reefs. *Soft Robot.* **3**, 23–33 (2016).
7. M. A. Graule, T. B. Clark, R. J. Wood, in *2022 IEEE/RSJ International Conference on Intelligent Robots and Systems (IROS)* (IEEE, 2022), pp. 719–726.
8. J. Hughes, U. Culha, F. Giardina, F. Guenther, A. Rosendo, F. Iida, Soft manipulators and grippers: A review. *Front. Robot. AI* **3**, 69 (2016).
9. M. Selvaggio, L. Ramirez, N. D. Naclerio, B. Siciliano, E. W. Hawkes, An obstacle-interaction planning method for navigation of actuated vine robots, in *2020 IEEE International Conference on Robotics and Automation (ICRA)* (IEEE, 2020), pp. 3227–3233.
10. M. M. Coad, L. H. Blumenschein, S. Cutler, Javier A. Reyna Zepeda, N. D. Naclerio, H. El-Hussieny, U. Mehmood, J.-H. Ryu, E. W. Hawkes, A. M. Okamura, Vine robots: Design, teleoperation, and deployment for navigation and exploration. arXiv:1903.00069 [cs.RO] (2019). https://doi.org/10.48550/arXiv.1903.00069.
11. D. A. Haggerty, N. D. Naclerio, E. W. Hawkes, Characterizing environmental interactions for soft growing robots, in *2019 IEEE/RSJ International Conference on Intelligent Robots and Systems (IROS)* (IEEE, 2019), pp. 3335–3342.
12. M. Wooten, C. Frazelle, I. D. Walker, A. Kapadia, J. H. Lee, Exploration and inspection with vine-inspired continuum robots, in *2018 IEEE International Conference on Robotics and Automation (ICRA)* (IEEE, 2018), pp. 5526–5533.
13. R. Colbaugh, H. Seraji, K. Glass, Direct adaptive impedance control of robot manipulators. *J. Robot. Syst.* **10**, 217–248 (1993).
14. R. Kelly, PD control with desired gravity compensation of robotic manipulators. *Int. J. Robot. Res.* **16**, 660–672 (1997).
15. B. J. Waibel, H. Kazerooni, Theory and experiments on the stability of robot compliance control. *IEEE Transact. Robot. Autom.* **7**, 95–104 (1991).
16. C. Della Santina, M. G. Catalano, A. Bicchi, Soft robots. *Encyclopedia Robot.* **489**, 1–15 (2020).
17. G. Chowdhary, M. Gazzola, G. Krishnan, C. Soman, S. Lovell, Soft robotics as an enabling technology for agroforestry practice and research. *Sustainability* **11**, 6751 (2019).
18. G. Robinson, J. B. C. Davies, in *Proceedings 1999 IEEE International Conference on Robotics and Automation (Cat. No. 99CH36288C)* (IEEE, 1999), vol. 4, pp. 2849–2854.
19. I. D. Walker, Continuous backbone "continuum" robot manipulators. *ISRN Robot.* **2013**, 1–19 (2013).
20. C. D. Remy, K. Buffinton, R. Siegwart, Energetics of passivity-based running with high-compliance series elastic actuation. *Int. J. Mechatron. Manuf. Syst.* **5**, 120–134 (2012).
21. B. Tondu, P. Lopez, The McKibben muscle and its use in actuating robot-arms showing similarities with human arm behaviour. *Ind. Rob.* **24**, 432–439 (1997).
22. B. Tondu, Modelling of the McKibben artificial muscle: A review. *J. Intell. Mater. Syst. Struct.* **23**, 225–253 (2012).
23. J. D. C. Pridham Jr., Bellows actuator, U.S. Patent 3,319,532 (1967).
24. J. Bishop-Moser, S. Kota, Design and modeling of generalized fiber-reinforced pneumatic soft actuators. *IEEE Transact. Robot.* **31**, 536–545 (2015).
25. F. Janabi-Sharifi, A. Jalali, I. D. Walker, Cosserat rod-based dynamic modeling of tendon-driven continuum robots: A tutorial. *IEEE Access* **9**, 68703–68719 (2021).
26. G. Grioli, S. Wolf, M. Garabini, M. Catalano, E. Burdet, D. Caldwell, R. Carloni, W. Friedl, M. Grebenstein, M. Laffranchi, D. Lefeber, S. Stramigioli, N. Tsagarakis, M. van Damme, B. Vanderborght, A. Albu-Schaeffer, A. Bicchi, Variable stiffness actuators: The user's point of view. *Int. J. Robot. Res.* **34**, 727–743 (2015).
27. N. G. Tsagarakis, I. Sardellitti, D. G. Caldwell, A new variable stiffness actuator (CompAct-VSA): Design and modelling, in *IEEE International Conference on Intelligent Robots and Systems* (IEEE, 2011), pp. 378–383.
28. F. Petit, M. Chalon, W. Friedl, M. Grebenstein, A. Albu-Schäffer, G. Hirzinger, Bidirectional antagonistic variable stiffness actuation: Analysis, design & Implementation, in *Proceedings IEEE International Conference on Robotics and Automation* (IEEE, 2010), pp. 4189–4196.
29. B. Vanderborght, A. Albu-Schaeffer, A. Bicchi, E. Burdet, D. G. Caldwell, R. Carloni, M. Catalano, O. Eiberger, W. Friedl, G. Ganesh, M. Garabini, M. Grebenstein, G. Grioli, S. Haddadin, H. Hoppner, A. Jafari, M. Laffranchi, D. Lefeber, F. Petit, S. Stramigioli, N. Tsagarakis, M. van Damme, R. van Ham, L. C. Visser, S. Wolf, Variable impedance actuators: A review. *Robot. Auton. Systems* **61**, 1601–1614 (2013).
30. A. Bicchi, G. Tonietti, M. Bavaro, M. Piccigallo, Variable Stiffness Actuators for Fast and Safe Motion Control, in *Robotics Research: The Eleventh International Symposium*, P. Dario, R. Chatila, Eds. (Springer, 2005), vol. 15, pp. 527–536.
31. R. Mengacci, M. Garabini, G. Grioli, M. G. Catalano, A. Bicchi, Overcoming the torque/stiffness range tradeoff in antagonistic variable stiffness actuators. *IEEE/ASME Trans. Mechatron.* **26**, 3186–3197 (2021).
32. A. Albu-Schäffer, S. Wolf, O. Eiberger, S. Haddadin, F. Petit, M. Chalon, Dynamic modelling and control of variable stiffness actuators, in *2010 IEEE International Conference on Robotics and Automation* (IEEE, 2010), pp. 2155–2162.

33. M. Keppler, D. Lakatos, C. Ott, A. Albu-Schäffer, Elastic Structure Preserving (ESP) control for compliantly actuated robots. *IEEE Transact. Robot.* **34**, 317–335 (2018).
34. M. Manti, V. Cacucciolo, M. Cianchetti, Stiffening in soft robotics: A review of the state of the art. *IEEE Robot. Autom. Mag.* **23**, 93–106 (2016).
35. F. Stella, J. Hughes, D. Rus, C. D. Santina, Prescribing Cartesian stiffness of soft robots by co-optimization of shape and segment-level stiffness. *Soft Robot.* **10**, 701–712 (2023).
36. R. J. Webster III, B. A. Jones, Design and kinematic modeling of constant curvature continuum robots: A review. *Int. J. Robot. Res.* **29**, 1661–1683 (2010).
37. L. U. Odhner, A. M. Dollar, The smooth curvature model: An efficient representation of Euler–Bernoulli flexures as robot joints. *IEEE Transact. Robot.* **28**, 761–772 (2012).
38. M. Wiese, K. Rüstmann, A. Raatz, Kinematic modeling of a soft pneumatic actuator using cubic hermite splines, in *2019 IEEE/RSJ International Conference on Intelligent Robots and Systems (IROS)* (IEEE, 2019), pp. 7176–7182.
39. S. Satheeshbabu, G. Krishnan, Designing systems of fiber reinforced pneumatic actuators using a pseudo-rigid body model, in *2017 IEEE/RSJ International Conference on Intelligent Robots and Systems (IROS)* (IEEE, 2017), pp. 1201–1206.
40. V. K. Venkiteswaran, J. Sikorski, S. Misra, Shape and contact force estimation of continuum manipulators using pseudo rigid body models. *Mech. Mach. Theory* **139**, 34–45 (2019).
41. R. K. Katzschmann, C. Della Santina, Y. Toshimitsu, A. Bicchi, D. Rus, Dynamic motion control of multi-segment soft robots using piecewise constant curvature matched with an augmented rigid body model, in *2019 2nd IEEE International Conference on Soft Robotics (RoboSoft)* (IEEE, 2019), pp. 454–461.
42. C. Armanini, F. Boyer, A. T. Mathew, C. Duriez, F. Renda, Soft robots modeling: A structured overview. arXiv:2112.03645 [cs.RO] (2021). https://doi.org/10.48550/arXiv.2112.03645.
43. M. A. Graule, C. B. Teeple, T. P. Mc Carthy, G. R. Kim, R. C. St Louis, R. J. Wood, Somo: Fast and accurate simulations of continuum robots in complex environments, in *2021 IEEE/RSJ International Conference on Intelligent Robots and Systems (IROS)* (IEEE, 2021), pp. 3934–3941.
44. M. A. Graule, T. P. McCarthy, C. B. Teeple, J. Werfel, R. J. Wood, SoMoGym: A toolkit for developing and evaluating controllers and reinforcement learning algorithms for soft robots. *IEEE Robot. Autom. Lett.* **7**, 4071–4078 (2022).
45. C. Ott, *Cartesian Impedance Control of Redundant and Flexible-Joint Robots* (Springer, 2008), pp. 29–44.
46. J. L. McKibben, "Artificial muscle" (Life, 1960), vol. 10, no. 10, pp. 87–88.
47. M. T. Gillespie, C. M. Best, M. D. Killpack, Simultaneous position and stiffness control for an inflatable soft robot, in *2016 IEEE International Conference on Robotics and Automation (ICRA)* (IEEE, 2016), pp. 1095–1101.
48. D. Bruder, C. D. Remy, R. Vasudevan, Nonlinear system identification of soft robot dynamics using koopman operator theory, in *2019 International Conference on Robotics and Automation (ICRA)* (IEEE, 2019), pp. 6244–6250.
49. D. Bruder, X. Fu, R. B. Gillespie, C. D. Remy, R. Vasudevan, Koopman-based control of a soft continuum manipulator under variable loading conditions. arXiv:2002.01407 [cs.RO] (2020). https://doi.org/10.48550/arXiv.2002.01407.
50. G. Olson, B. Woronowicz, Y. Mengüç, Characterization of a class of soft bending arms, in *2019 2nd IEEE International Conference on Soft Robotics (RoboSoft)* (IEEE, 2019), pp. 462–469.
51. M. D. Grissom, *Unmanned Systems Technology VIII* (International Society for Optics and Photonics, 2006), vol. 6230, p. 62301F.
52. M. W. Spong, Control of robot manipulators, in *The control handbook* (CRS Press, 1996), vol 144, p. 1339.
53. D. Bruder, R. J. Wood, The chain-link actuator: Exploiting the bending stiffness of Mckibben artificial muscles to achieve larger contraction ratios. *IEEE Robot. Autom. Lett.* **7**, 542–548 (2022).
54. E. Coumans, Y. Bai, Pybullet, a python module for physics simulation for games, robotics and machine learning (2016–2019); http://pybullet.org.
55. A. J. Cohen, M. Kollosche, M. C. Yuen, D.-Y. Lee, D. R. Clarke, R. J. Wood, *Adv. Funct. Mater.* **32**, 2205394 (2022).
56. J. Poccard-Saudart, S. Xu, C. B. Teeple, N. S. P. Hyun, K. P. Becker, R. J. Wood, Controlling soft fluidic actuators using soft DEA-based valves. *IEEE Robot. Automat. Lett.* **7**, 8837–8844 (2022).
57. D. Popov, I. Gaponov, J.-H. Ryu, Towards variable stiffness control of antagonistic twisted string actuators, in *2014 IEEE/RSJ International Conference on Intelligent Robots and Systems* (IEEE, 2014), pp. 2789–2794.
58. D. Bombara, R. Konda, S. Swanbeck, J. Zhang, Anthropomorphic twisted string-actuated soft robotic gripper with tendon-based stiffening. arXiv:2207.03603 [cs.RO] (2022). https://doi.org/10.48550/arXiv.2207.03603.
59. M. W. Hannan, I. D. Walker, Kinematics and the implementation of an elephant's trunk manipulator and other continuum style robots. *J. Robot. Syst.* **20**, 45–63 (2003).
60. J. M. Winters, L. Stark, Analysis of fundamental human movement patterns through the use of in-depth antagonistic muscle models. *IEEE Trans. Biomed. Eng.* **BME-32**, 826–839 (1985).
61. A. Stilli, H. A. Wurdemann, K. Althoefer, Shrinkable, stiffness-controllable soft manipulator based on a bio-inspired antagonistic actuation principle, in *2014 IEEE/RSJ International Conference on Intelligent Robots and Systems* (IEEE, 2014), pp. 2476–2481.
62. F. Maghooa, A. Stilli, Y. Noh, K. Althoefer, H. A. Wurdemann, Tendon and pressure actuation for a bio-inspired manipulator based on an antagonistic principle, in *2015 IEEE International Conference on Robotics and Automation (ICRA)* (IEEE, 2015), pp. 2556–2561.
63. R. Kang, D. T. Branson, T. Zheng, E. Guglielmino, D. G. Caldwell, Design, modeling and control of a pneumatically actuated manipulator inspired by biological continuum structures. *Bioinspir. Biomim.* **8**, 036008 (2013).

Acknowledgments

Funding: This work was supported by a Space Technology Research Institutes grant (number 80NSSC19K1076) from NASA's Space Technology Research Grants Program. **Author contributions:** D.B. formulated the main ideas, designed and performed the real-world experiments, and wrote the manuscript. M.A.G. developed the simulation tools, implemented the simulation experiments, revised the manuscript, and refined ideas. C.B.T. designed and built the pneumatic control system and software tools used in the real-world experiments. R.J.W. contributed to the analysis of results, revised the manuscript, and refined ideas. **Competing interests:** The authors declare that they have no competing interests. **Data and materials availability:** All data needed to evaluate the conclusions in the paper are present in the paper or can be accessed using the following DOI: 10.5281/zenodo.8194080.

Submitted 20 November 2022
Accepted 2 August 2023
Published 30 August 2023
10.1126/scirobotics.adf9001

Science Robotics

Increasing the payload capacity of soft robot arms by localized stiffening

Daniel Bruder, Moritz A. Graule, Clark B. Teeple, and Robert J. Wood

Sci. Robot. **8** (81), eadf9001. DOI: 10.1126/scirobotics.adf9001

Science Robotics (ISSN 2470-9476) is published by the American Association for the Advancement of Science. 1200 New York Avenue NW, Washington, DC 20005. The title *Science Robotics* is a registered trademark of AAAS.